

3 **Basement topography and sediment thickness beneath Antarctica's Ross Ice Shelf**4 M.D. Tankersley<sup>1,2</sup>, H.J. Horgan<sup>1</sup>, C.S. Siddoway<sup>3</sup>, F. Caratori Tontini<sup>2,4</sup>, K.J. Tinto<sup>5</sup>5 <sup>1</sup>Antarctic Research Centre, Victoria University of Wellington, Wellington, New Zealand6 <sup>2</sup>GNS Science, Lower Hutt, New Zealand7 <sup>3</sup>Colorado College, Colorado Springs, CO, USA8 <sup>4</sup>University of Genoa, Genoa, Italy9 <sup>5</sup>Lamont-Doherty Earth Observatory, Columbia University, Palisades, NY, USA10 **Contents of this file**

11 Text S1 to S6

12 Table S1

13 Figures S1 to S5

14 **Introduction**

15 This supplement provides additional information on the collection and processing of  
16 aeromagnetic line data (**Text S1**), the methodology of tying ROSETTA-Ice magnetic  
17 basement to ANTOSTRAT acoustic basement (Brancolini et al., 1995), through the use of  
18 Operation IceBridge( OIB) magnetic data (Cochran et al. 2014) (**Text S2 and S3**), the  
19 gridding, merging, and filtering of the resulting basement grid (**Text S4**), the calculation  
20 of sediment thickness and  $\beta$ -factors for the region (**Text S5**), and our quantification of  
21 uncertainties and comparison with points of previously measured sediment thickness  
22 (**Text S6**). Sediment thickness comparisons with past seismic surveys are included in  
23 **Table S1**. Also included are supplementary figures showing various additional Ross Ice  
24 Shelf grids (**Figure S1**), the Werner deconvolution solutions of OIB flight 403.3 (**Figure**  
25 **S2**), several selected ROSETTA-Ice flight lines with Werner deconvolution solutions  
26 (**Figure S3**), unfiltered basement solutions with flight line locations and individual  
27 Werner deconvolution solutions (**Figure S4**), and uncertainties applied to basement and  
28 sediment thickness results (**Figure S5**). Python code, within a Jupyter notebook,  
29 documents our workflow and figure creation, and is accessible here:  
30 <https://zenodo.org/badge/latestdoi/470814953>

## 31 **Text S1. Magnetic data collection, processing, and Werner deconvolution**

32 Both ROSETTA-Ice and OIB data sets were collected with a Scintrex CS3 Cesium  
33 magnetometer. Average flight speeds were 123 m/s and 93 m/s for OIB and ROSETTA-  
34 Ice respectively. Altitudes for the sections of OIB flight 403 used here average around  
35 400 m above sea level, while ROSETTA-Ice altitude averaged at 750 m above ground  
36 level. OIB data were resampled from 20Hz to 1Hz to match the frequency of the  
37 ROSETTA-Ice data. Both datasets have been despiked, diurnally corrected, and had the  
38 International Geomagnetic Reference Field model removed. See Tinto et al. (2019) for  
39 more details of the ROSETTA-Ice survey and flight line locations. Due to variable flight  
40 elevations, both between and within the datasets, all magnetic data were upward-  
41 continued to 1000 m above sea level. To avoid artefacts of downwards continuing, any  
42 data with flight elevations above 1000 m were removed.

43 Here we use 2D Werner deconvolution (Werner, 1953, Ku & Sharp, 1983), applied to  
44 aeromagnetic line data, to image the shallowest magnetic signals in the crust. Assuming  
45 that the overlying sediments produce smaller magnetic anomalies than the crystalline  
46 basement, we treat the resulting solutions as a depth to the magnetic basement. During  
47 Werner deconvolution, moving and expanding windows are passed over the magnetic  
48 anomaly line data. Within each window, after linearly detrending the data, the source  
49 parameters of the anomalies are estimated with a least-squares approach, assuming the  
50 source bodies are infinite-depth dikes or contacts. The source parameters include  
51 position (distance along profile and depth), magnetic susceptibility, and source geometry  
52 (contact or dike). Solutions are considered valid between 1200 m and 20 km of upward  
53 continued flight elevation (approx. 200 m - 19 km bsl). Windows ranged from 500 m - 50  
54 km, with a window shift increment of 1 km and an expansion of 1 km.

55 Due to passing over the data many times with varying window widths, Werner  
56 deconvolution produces a depth-scatter of solutions, which tend to cluster vertically  
57 beneath the true magnetic sources. Each of these solutions consists of location, depth,  
58 susceptibility ( $S$ ), window width ( $W$ ), and a simplified source geometry (dike or contact).  
59 For contact-type solutions, parameter  $S$  is the estimated magnetic susceptibility of the  
60 body, while for dike-type solutions,  $S$  is the product of susceptibility and dike width.  
61 During filtering (Text S2-3), a cut-off based on parameter  $S$  is used to remove shallow  
62 solutions. Since the value of parameter  $S$  for contact solutions are typically much smaller  
63 than for dike solutions (since they are not multiplied by dike width), only dike solutions  
64 have been considered here. To achieve a basement surface from this resulting depth-  
65 scatter of solutions, we have utilized parameter-based filtering and clustering, described  
66 in Text S2-3. This Werner deconvolution process was the same for both OIB and  
67 ROSETTA-Ice magnetics data. Werner deconvolution was performed in Geosoft's Oasis  
68 Montaj and subsequent processing of these results was performed in Python, and is  
69 included in a Jupyter notebook; <https://zenodo.org/badge/latestdoi/470814953>.

70 This magnetic basement approach has been used to map sedimentary basins  
71 throughout Antarctica, including the Ross Sea (Karner et al., 2005), western Marie Byrd  
72 Land (Bell et al., 2006), and Wilkes Subglacial Basin (Studinger et al., 2004; Frederick et al.,  
73 2016). Our approach is similar to past studies, but our proximity to well-constrained  
74 offshore seismic basement depths (Brancolini et al., 1995) allows us to develop the  
75 method further. Most studies display their results as 2D profiles with the depth-scatter of

76 solutions mentioned above, and simply use the tops of the clusters as the basement  
77 depth. By comparison with seismic basement, we have developed a reliable, automated  
78 method of 'draping' a surface over these depth-scattered solutions to produce a 3D  
79 surface. This process is described below.

## 80 **Text S2. Tying magnetic basement to seismic basement**

81 To validate this method and address uncertainty we perform Werner deconvolution  
82 for OIB magnetics data (Figure 1b, Cochran et al., 2014) over the Ross Sea. Here, ice-free  
83 conditions have permitted shipborne seismic surveys to image basement depths in the  
84 region. These have been compiled by the Antarctic Offshore Acoustic Stratigraphy  
85 project (ANTOSTRAT) (Brancolini et al., 1995) (Figure 1b). The basement was not imaged  
86 for the deeper portions of the basins and data coverage of actual basement reflectors,  
87 versus interpolation between basement reflectors, is not reported. Werner deconvolution  
88 (Text S1) produces a series of many solutions (black dots in Figures 2 & S2) at each  
89 window along the line.

90 To achieve a basement surface, instead of a depth-scatter of solutions, solutions  
91 were filtered based on Werner window width ( $W$ ) and the product of magnetic  
92 susceptibility and body width (parameter  $S$ ). Filtered solutions (black circles, scaled to  
93 parameter  $S$  in Figures 2 & S2) were then horizontally binned with variable bin sizes  
94 (parameter  $B$ ) (vertical grey lines in Figures 2 & S2). Bins with a minimum count of  
95 solutions (parameter  $C$ ) were retained, and the depth of the bin center was set to the  
96 95<sup>th</sup>-percentile depth of the solutions in the bin. This removed spurious shallow  
97 solutions, while effectively retaining the 'top' of the magnetic signal. These bin centers  
98 (orange crosses in Figures 2 & S2) were then interpolated, producing our model of  
99 magnetic basement depths (orange line in Figures 2 & S2). The above filtering  
100 techniques removed the solutions above the basement, and the clustering technique  
101 fitted a surface over the remaining points, which represents the top of the basement.  
102 This interpolated line allowed a direct comparison between ANTOSTRAT seismic  
103 basement and OIB magnetic basement.

104 We varied each of the four parameters ( $W$ ,  $S$ ,  $B$ , and  $C$ ) with 21 different values and  
105 conducted the above procedures for all unique combinations of them on OIB line 403,  
106 segments 1 and 3, in the Ross Sea (location in Figure 1b). This resulted in 194,481  
107 iterations, for each of which we calculated a mean absolute difference at points every  
108 5km between ANTOSTRAT seismic basement and the resulting OIB magnetic basement.  
109 We found the parameter values which produced the closest match between OIB  
110 magnetic basement and ANTOSTRAT seismic basement, as shown in Figures 2 & S2.  
111 These resulting values were a maximum Werner deconvolution window width (parameter  
112  $W$ ) of 10 km, a minimum product of magnetic susceptibility and body width (parameter  
113  $S$ ) of 1.0, a horizontal bin width (parameter  $B$ ) of 36 km, and a minimum number of  
114 solutions per bin (parameter  $C$ ) of 6. The median absolute misfit between OIB and  
115 ANTOSTRAT basement for the two line-segments was 480 m (270 m for Line 403-1  
116 (Figure 2), and 1060 m for Line 403-3 (Figure S2)). This equates to 11% of ANTOSTRAT  
117 depths. The close fit between the OIB magnetic basement and the ANTOSTRAT seismic  
118 basement both supports the validity of this method and gives us the parameters  
119 necessary to repeat this method for data over the RIS.

120 **Text S3. Tying Ross Sea magnetic basement to Ross Ice Shelf magnetic basement**

121 Having optimized our method to match OIB magnetic basement to ANTOSTRAT  
122 seismic basement in the Ross Sea (Text S2, Figures 2 & S2), we now optimize the method  
123 to match ROSETTA-Ice magnetic basement to OIB magnetic basement. This additional  
124 optimization is necessary due to differences in processing and survey design, including  
125 flight elevations, speed, aircraft, mounting equipment used, and frequency of recording.  
126 With the optimized parameters for OIB data (Text S2), we calculate magnetic basement  
127 for OIB flight 404 over the ice shelf. We treat this as the 'true' basement and update the  
128 filtering and clustering parameters (Text S1) to minimize the misfit between OIB  
129 basement and the resulting ROSETTA-Ice basement. This tuning was performed on  
130 ROSETTA-Ice lines 590 and 650, which were coincident with segments from OIB line 404  
131 (location in Figures 1b & S4). Optimal parameters to match ROSETTA-Ice solutions to  
132 OIB basement are found to be  $W < 26$  km,  $S > 1.2$ ,  $B = 36$  km, and  $C > 40$ , resulting in a  
133 median absolute misfit between OIB basement and ROSETTA-Ice solutions of 400 m  
134 (22% of OIB depth). With these parameters which best match ROSETTA magnetic  
135 basement to OIB magnetic basement, we performed the same procedure on all the  
136 ROSETTA-ice flight lines. A selection of these lines, and the two ties to OIB 404, are  
137 shown in Figure S3.

138 **Text S4. Gridding, merging, and filtering**

139 The above processes were performed on all ROSETTA-ice flight lines (white lines in  
140 Figure S4), including the N-S tie lines at  $\sim 55$  km spacing. Where the tie lines crossed  
141 over the E-W flights lines, some resulting basement solutions (black dots in Figure S4)  
142 are nearby those from the crossing line. Since we are interested in the shallowest  
143 magnetic signals, we have retained only the shallowest solution with 8km cells across our  
144 region. Since bin widths (parameter B) were set to 36 km, the nearest solutions along  
145 individual lines were further apart than the 8km cell. The closest spacing of E-W flight  
146 lines was 10 km, so this process only affected solutions at the crossover between N-S  
147 and E-W lines. These points were then gridded with a 5 km cell size and a minimum  
148 curvature spline with a tension factor of 0.35 (Smith & Wessel, 1990) (Figure S4). This  
149 grid was then merged with a Ross Sea seismic basement grid. The Ross Sea grid, while  
150 mostly ANTOSTRAT data, was sourced from a regional compilation of sediment  
151 thicknesses (Lindeque et al., 2016, Wilson and Luyendyk 2009), we have subtracted from  
152 bathymetry depths (Morlighem et al. 2020) to achieve basement depths. Where the grids  
153 overlap near the ice shelf edge, we retain our RIS values. To aid in the merging at the  
154 overlaps, and to match RIS basement wavelengths to the characteristic basement  
155 wavelengths of ANTOSTRAT, we filtered the merged grid with an 80 km Gaussian filter  
156 (Figure 3a). This filtering was performed with a variety of wavelengths (20-120 km),  
157 where we found filters  $< 80$  km didn't significantly alter the regional basement, while  
158 filters  $> 80$  km excessively smoothed the basement topography.

159 **Text S5. Sediment thickness and  $\beta$ -factor calculations**

160 With the regional basement model (Figure 3a) including RIS magnetic basement  
161 and offshore seismic basement, we calculated sediment thickness (Figure 3b) by  
162 subtracting the grid from Bedmachine bathymetry depths (Figure 1a & S1e, Morlighem et

163 al. 2020). Previous estimates of sediment thickness for the sub-RIS come from the  
164 extrapolation of gravity anomalies with bathymetry trends (Wilson and Luyendyk, 2009).  
165 These were included in the Lindeque et al. (2016) compilation (Figure S1d). Eocene-  
166 Oligocene boundary paleotopographic reconstructions (Wilson et al., 2012, Paxman et  
167 al., 2019) assumed this sediment estimate was post-Eocene and used it as their  
168 maximum sub-RIS sediment thickness, incorporated into their minimum surface  
169 reconstruction. The thickness of sediment affects onshore erosion estimates, surface  
170 raising due to deposition, and isostatic surface subsidence to due loading. For their  
171 maximum paleotopographic reconstructions, they used a thinner sediment model, with  
172 the same general trends (Wilson & Luyendyk, 2009). Figure S1 (c, d, & f) shows the  
173 comparison between the sediment thickness models. Figure S1f colorbar histogram  
174 shows the distribution, with our values having a mean thickness ~115m greater than the  
175 past model. Yet, along the Siple Coast, we show much greater discrepancies, up to 2 km  
176 thicker.

177  $\beta$ -factor, the ratio of initial crustal thickness to final crustal thickness, is useful for  
178 quantifying the thinning of crust in extensional settings. We calculate a distribution of  $\beta$ -  
179 factors beneath the RIS by assuming a uniform initial crustal thickness and dividing it by  
180 current crustal thickness. We pick an initial crustal thickness of 38 km, which represents a  
181 global average for un-thinned plateau-type crust (Mooney et al., 1998), and has been  
182 used for the West Antarctic Rift System  $\beta$ -factor calculations (Müller et al., 2007). For the  
183 final (current) crustal thickness, we use a continent-wide Moho model from surface wave  
184 observations to define the bottom of the crust (An et al., 2015). For the top of the crust,  
185 we use our resulting RIS basement grid.

## 186 **Text S6. Uncertainty and assumptions**

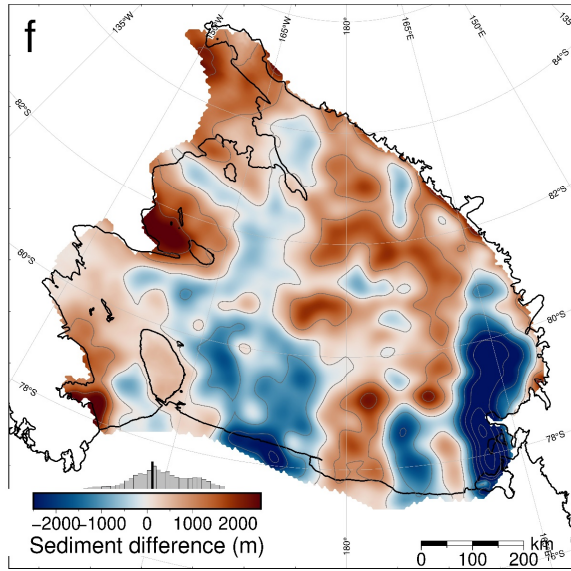
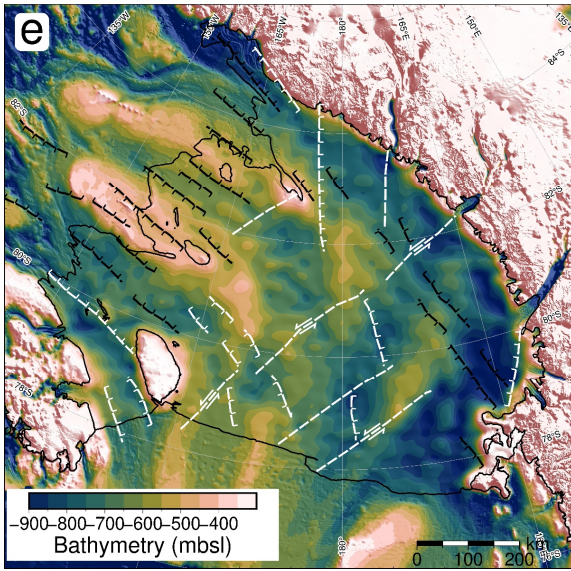
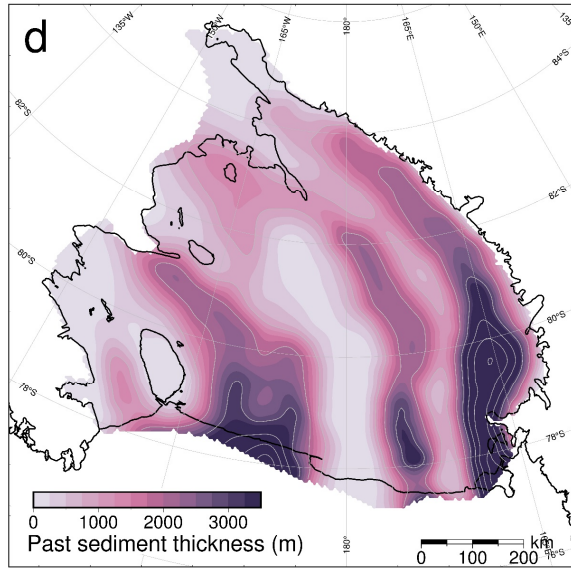
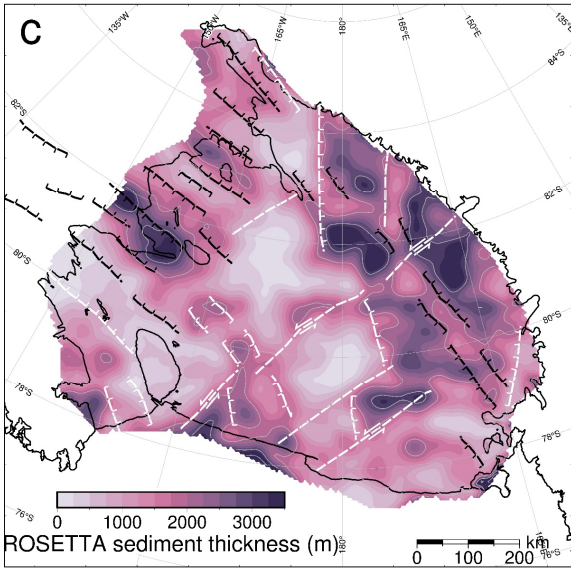
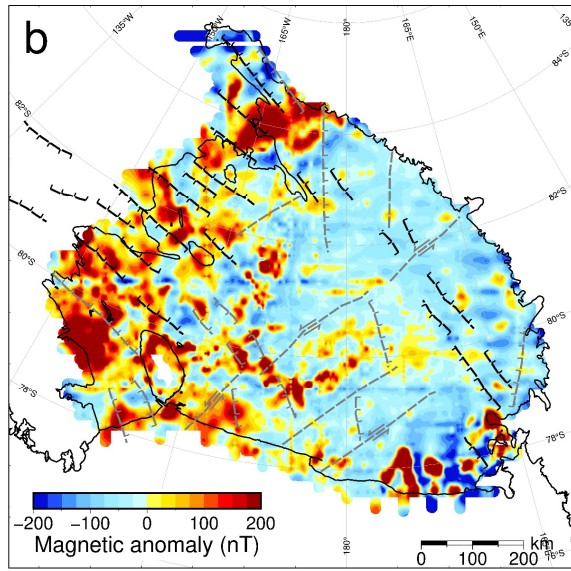
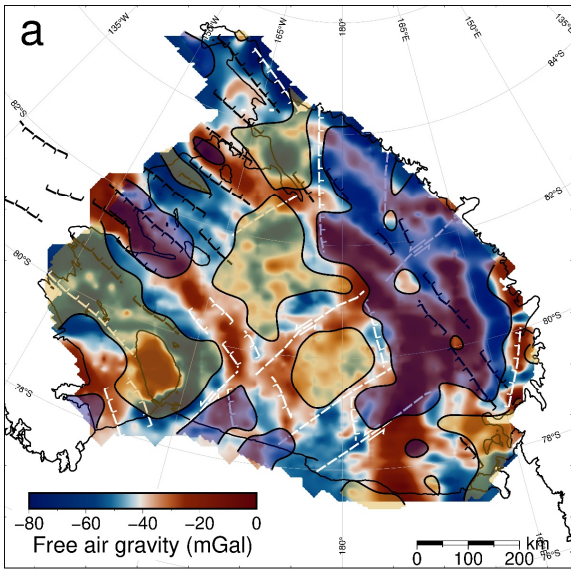
187 We estimated a representative uncertainty for our basement model by examining  
188 the misfit of our modeled basement compared to offshore seismic basement depths  
189 (Brancolini et al., 1995). We did this by sampling our OIB magnetic basement estimate  
190 and the coincident ANTOSTRAT basement at 1 km intervals along lines 403-1 and 403-3  
191 (Figures 2 and S2) and compared the values. The resulting absolute values of the  
192 differences don't exhibit a normal distribution; therefore, we use the median of the  
193 absolute misfit (+/-480m) as the basement model uncertainty. This equates to 22% of  
194 average basement depths for the sub-RIS. We performed a similar analysis between OIB  
195 magnetic basement and ROSETTA-Ice magnetic basement for coincident lines 590 and  
196 650 (Figure S3 e & f). This resulted in a median absolute misfit of 400m. Tinto et al.  
197 (2019) report an uncertainty of 68m for their bathymetry model. Incorporating this with  
198 our basement model gives an uncertainty of 550m (37% of average thickness) for our  
199 sediment thickness results. Comparison with sub-RIS sediment thickness and distribution  
200 results from a variety of methods, including active source seismic surveys (Table S1 and  
201 references within), seismic radial anisotropy (Zhou et al., 2022), geophysical machine  
202 learning (Li et al. 2021), and magnetotelluric surveying (Gustafson et al. 2022, in review),  
203 all show general agreement with our results.

204 Our resulting basement grid is the depth to the shallowest magnetic signal. It is  
205 assumed that the crystalline basement in this region produces significantly larger  
206 magnetic anomalies compared to the overlying sediment fill. Note that in some

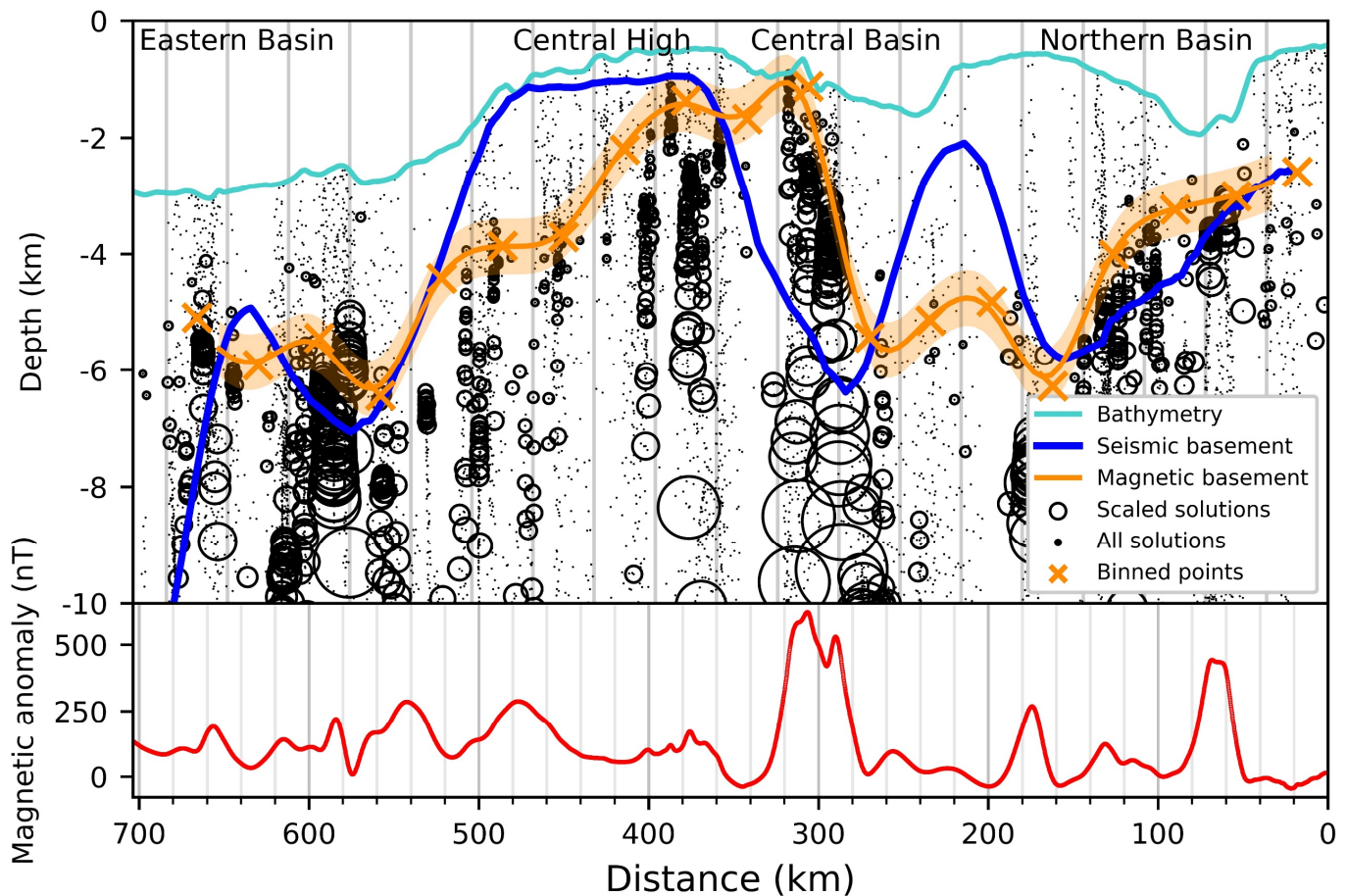
207 instances, such as igneous bodies intruded into sedimentary basin fill, Werner-  
 208 determined solutions fall upon the crest of the intrusion, and the actual top of the  
 209 crystalline basement could be at a deeper level. Intrusions of small lateral extent will have  
 210 small widths, resulting in small values of parameter S (susceptibility x width) and  
 211 therefore will be removed by our filter (Text S2). For larger intrusions into existing basins,  
 212 (i.e. Ross Island and Minna Bluff (Cox et al., 2019)), the modeled magnetic basement  
 213 surface will be shallower than the bottom of the sedimentary basin. While this  
 214 underestimates sediment volume, it better characterizes the competency of the substrate  
 215 from an ice dynamics perspective. This is similar to how extensive intrusions into basins  
 216 would be imaged by seismic surveys as shallow basement. However, these extensive  
 217 regions of late-Cretaceous-Cenozoic magmatism are not expected to be prevalent under  
 218 the RIS (Andrews et al., 2021).

Name	Reference	Seismic sediment thickness (m)	Magnetic sediment thickness (m)	Absolute difference (m)
CIR	Rooney et al. (1987)	400	504	104
I10S	Robertson and Bentley (1989)	750+/-100	1624	874
J9DC	Greischar et al. (1992)	1350	771	579
BC	Robertson and Bentley (1989)	1900+/-400	1124	776
RI	Greischar et al. (1992)	850	807	43
C49	Crary (1961)	754	1162	408
LAS	Crary (1961)	1325	1820	495
Q13	Greischar et al. (1992)	255+/-145	744	489

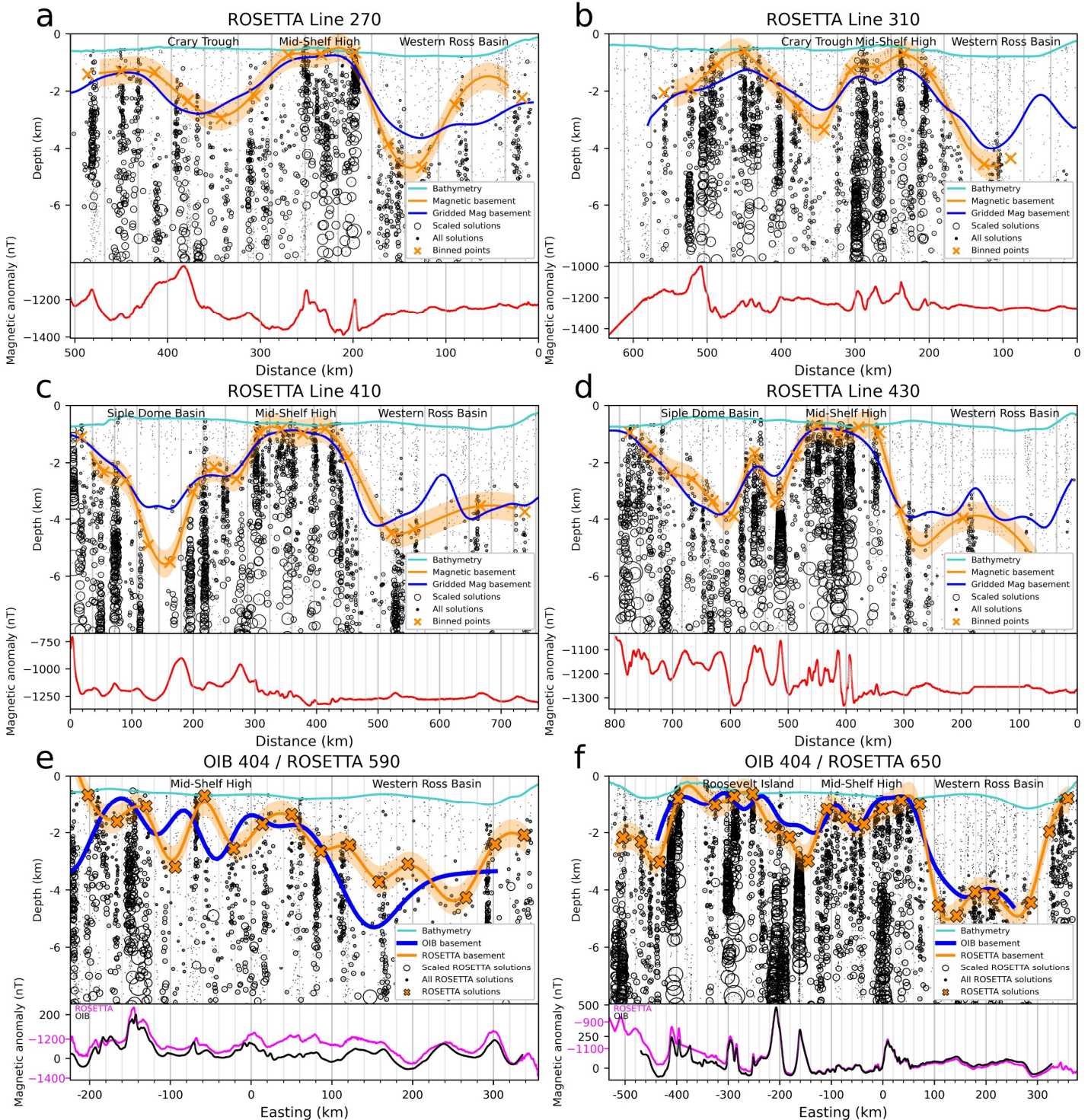
219 **Table S1.** Previous seismic sediment thickness results for the Ross Ice Shelf. Stations  
 220 names are labeled in Figure 3b. Magnetic sediment thickness column shows our sampled  
 221 results at the location of each station. Comparing the seismic estimates with our  
 222 sediment thickness at the eight stations gives a median absolute misfit of 480m.



223 **Figure S1.** (a) ROSETTA-Ice free air gravity (Tinto et al., 2019). Shaded yellow regions are  
 224 shallow basement (<~1600 mbsl), shaded blue regions are deep basement (>~2600  
 225 mbsl). (b) ROSETTA-Ice airborne magnetic anomaly data (Tinto et al., 2019). (c)  
 226 Sediment thickness from this study (same as Figure 3b), with 1 km contours. (d)  
 227 Sediment thickness from a regional compilation (Text S5, Lindeque et al., 2016, Wilson &  
 228 Luyendyk, 2009), with 1 km contours. (e) Bedmachine2 bathymetry (Morlighem et al.,  
 229 2020), from which sediment thickness in (c) was calculated. (f) Difference between (c)  
 230 and (d). Red signifies our results have more sediment, while blue signifies our results  
 231 have less sediment. Histogram shows data distribution, with mean value (black) at 115m.  
 232 Inferred faults in a),b),c), and e) same as Figure 4a. Grounding line and coastlines in black  
 233 (Rignot et al., 2013). Projection is Antarctic Polar Stereographic: EPSG 3031.

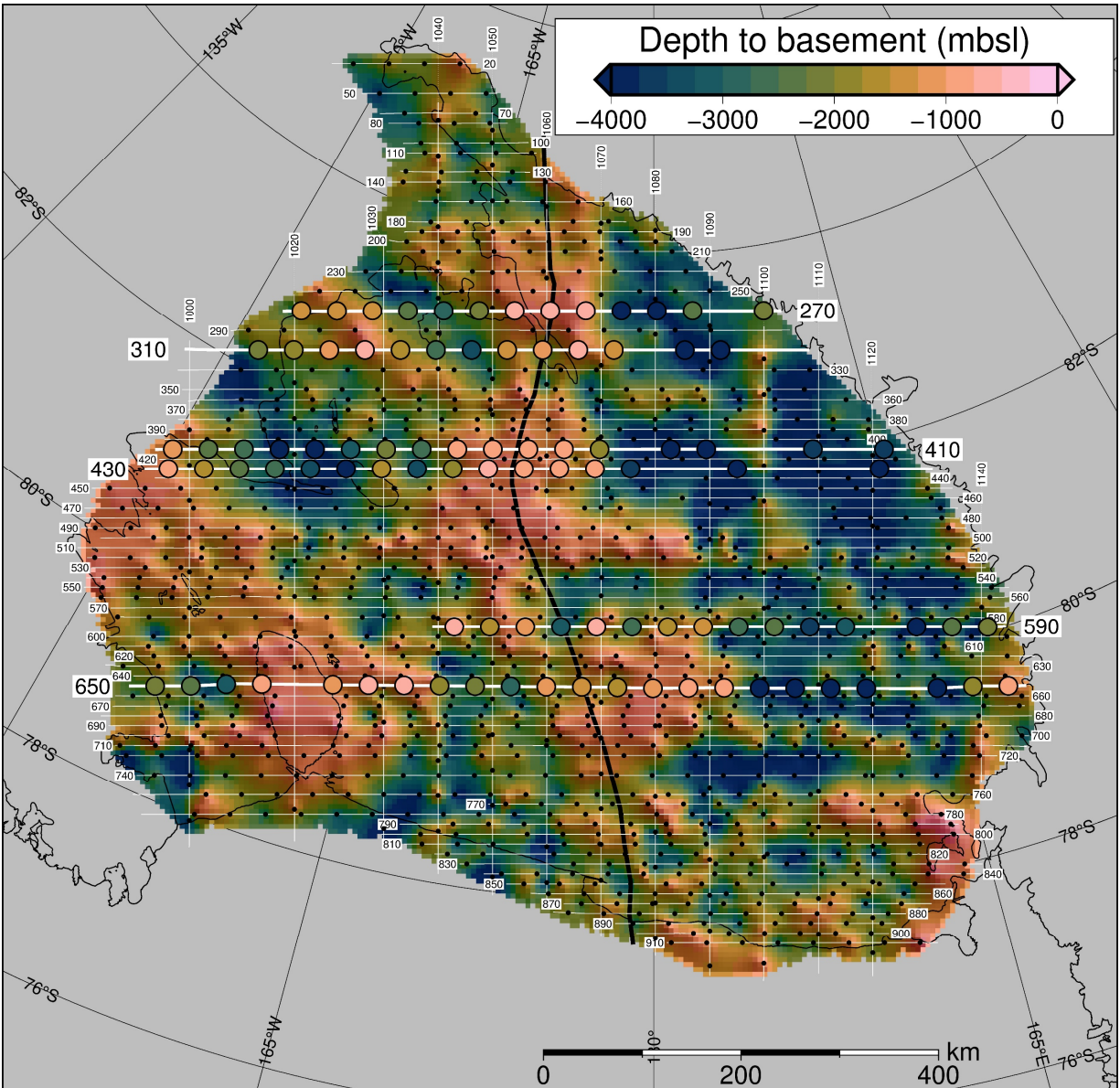


234 **Figure S2.** Ross Sea magnetic and seismic basement comparison. Operation IceBridge  
 235 airborne magnetic data (lower panel) from segment 403-3 (Figure 1b). Small dots show  
 236 Werner deconvolution solutions, which were filtered based on parameter S and W (Text  
 237 S1) to produce black circles, which are scaled to parameter S. These circles were binned  
 238 at a width equal to parameter B, shown by the vertical grey lines in the upper panel.  
 239 Orange crosses show bin centers, which were fitted to a line to facilitate the comparison  
 240 between the magnetic basement (orange line) and seismic basement (blue line). Orange  
 241 band shows +/- 480m uncertainty for the basement model. Ross Sea basement features  
 242 are labeled on top.

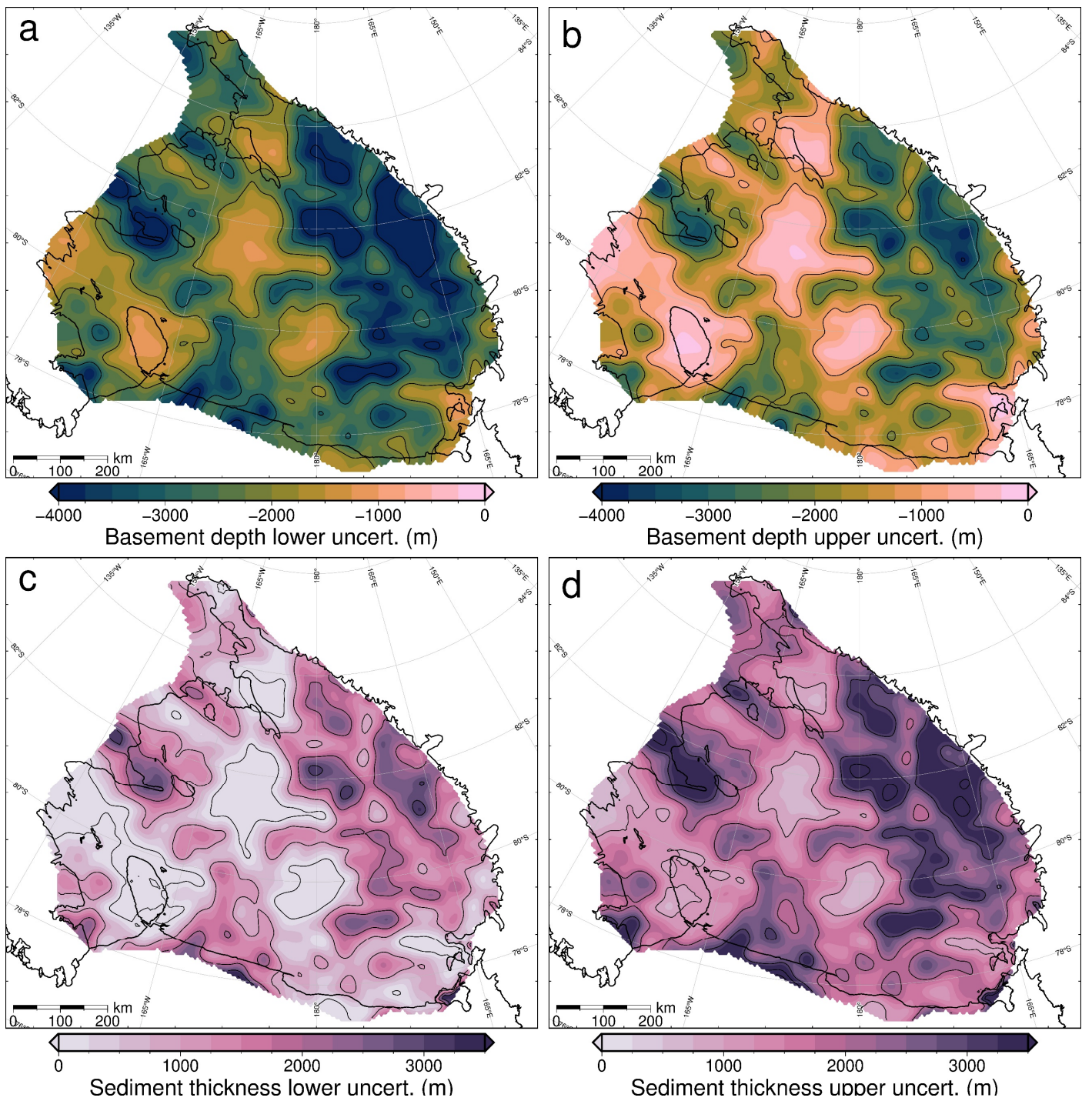


243 **Figure S3.** Werner deconvolution solutions for a selection of ROSETTA-Ice lines,  
 244 locations highlighted in Figure S4. Bathymetry from Bedmap2 (Fretwell et al., 2013). Dots,  
 245 circles, and vertical grey lines same as Figure S2. **a-d)** Comparison between magnetic  
 246 basement before and after filtering and gridding. Orange crosses are magnetic basement  
 247 solutions, shown as black dots in Figure S4, and highlighted for these lines. Orange line  
 248 with uncertainty bounds is fitted to these solutions. Blue lines are magnetic basement

249 sampled from the grid of Figure 1a, after gridding and filtering. Red lines show  
 250 ROSETTA-Ice magnetics data. **e-f)** Comparison between magnetic basement resulting  
 251 from Werner deconvolution of coincident OIB and ROSETTA-Ice flight lines. Location is  
 252 shown in Figures 1b and S4. These two lines were used to tie the ROSETTA-Ice survey to  
 253 the OIB survey (Text S3). Blue lines are OIB magnetic basement results, orange crosses  
 254 and fitted orange lines with uncertainty bands are ROSETTA-Ice magnetic basement.  
 255 ROSETTA-Ice (pink) and OIB (black) magnetics data are shown in lower panels.



256 **Figure S4.** Unfiltered magnetic basement. Point solutions (black dots here, orange  
 257 crosses in Figure S3) along ROSETTA-Ice flight lines (labeled) were gridded with a 5km  
 258 cell size and a minimum curvature spline with a tension factor of 0.35. Figure S3 flight  
 259 lines (bold white) and point solutions (colored circles) are shown. Black line through the  
 260 Mid-Shelf High shows the East-West Antarctic divide used in colorbar histograms of  
 261 Figures 3 and 4a. Grounding line and coastlines in black (Rignot et al., 2013).



262 **Figure S5.** Upper and lower limits of uncertainty applied to **a-b)** magnetic basement and  
 263 **c-d)** sediment thickness. See Text S6 for how these uncertainties were determined.